Introducing a new metrics for the atmospheric pressure adjustment to thermal structures at the ocean surface

Agostino N. Meroni[1], Fabien Desbiolles[1,2]and Claudia Pasquero[1]

[1]Department of Earth and Environmental Sciences, University of Milano-Bicocca, Milan, 20126, Italy
[2]Osservatorio Geofisico Sperimentale, Trieste, Italy

Key Points:

- The standard metrics for the pressure adjustment mechanism is adversely affected by advection
- Pressure is a scalar and secondary pressure gradients are generated in all directions
- The pressure adjustment is detectable in the direction perpendicular to the background wind

Corresponding author: Agostino N. Meroni, agostino.meroni@unimib.it

Abstract

Thermal structures at the sea surface are known to affect the overlying atmospheric dynamics over various spatio-temporal scales, from hourly and sub-kilometric to annual and $O(1000$ km). The relevant mechanisms at play are generally identified by means of correlation coefficients (in space or time) or by linear regression analysis using appropriate couples of variables. For fine spatial scales, where SST gradients get stronger, the advection might disrupt these correlations and, thus, mask the action of such mechanisms, just because of the chosen metrics. For example, at the oceanic sub-mesoscale, around 1-10 km and hourly time scales, the standard metrics used to identify the pressure adjustment mechanism (that involves sea surface temperature, SST, Laplacian and wind divergence) may suffer from this issue, even for weak wind conditions. By exploiting high-resolution realistic numerical simulations with *ad hoc* SST forcing fields, we introduce some new metrics to evaluate the action of the pressure adjustment atmospheric response to the surface oceanic thermal structures. It is found that the most skillful metrics is based on the wind divergence and SST second spatial derivative evaluated in the across direction of a locally defined background wind field.

Plain Language Summary

The ocean surface is characterized by a wealth of warm and cold structures that are known to influence the overlying atmospheric flow through different mechanisms. One of these mechanisms involves the variation of sea level pressure that can drive secondary wind circulations according to how the sea surface temperature is distributed in space. To assess whether this mechanism is in action, the co-location of sea temperature maxima (or minima) with zones of wind convergence (divergence) is generally considered. However, the presence of the wind itself has been shown to displace and delay the wind response so that there are cases where the pressure field responds to the sea temperature forcing but this is not detected by the standard metrics. Since pressure variability is generated in all directions, we propose to measure this kind of wind response in the direction perpendicular to the background wind in order to avoid the masking effect of the background wind.

1 Introduction

Sea surface temperature (SST) structures are known to affect the marine atmospheric boundary layer (MABL) dynamics via two main mechanisms: the Downward Momentum Mixing (DMM) mechanism (Hayes et al., 1989; Wallace et al., 1989) and the Pressure Adjustment (PA) one (Lindzen & Nigam, 1987). In the DMM physics, spatial variations of SST modulate the atmospheric stability and the vertical mixing of horizontal momentum, resulting in an acceleration (deceleration) of the surface wind over relatively warm (cold) SST patches. In the PA physics, instead, the air thermal expansion (contraction) over warm (cold) SST patches is responsible for a spatial modulation of the sea level pressure field that, through secondary pressure gradients, drives surface wind convergence (divergence) over warm (cold) SST structures.

The atmospheric response mediated by these two mechanisms has been observed over different time scales and different regions of the world. Notable examples of observations and theoretical modeling of the MABL atmospheric response over annual and multi-annual scales are the works of Minobe et al. (2008) and Takatama et al. (2015), that focus on the PA-mediated atmospheric response over the Gulf Stream. In the same region, and over the other western boundary currents, a wealth of works have highlighted the prominent role of the DMM on multi-annual (Chelton et al., 2004), seasonal and monthly time scales (Small et al., 2008, and references therein). On the one hand, on scales of the order of few days or even shorter, the works by Chelton et al. (2001), Frenger et al. (2013) and Gaube et al. (2019), for example, have shown that the DMM controls the fast

atmospheric response over the Tropical Instability Waves of the eastern Pacific cold tongue, over Southern ocean mesoscale eddies and over a sub-mesoscale filament of the Gulf Stream, respectively. Meroni et al. (2020) and Desbiolles et al. (2021), by looking at 25 years of satellite and reanalysis data, have highlighted the prominent role of the DMM on daily scales in affecting both the surface wind response, and the subsequent cloud and precipitation signature over SST fronts in the Mediterranean Sea. On the other hand, the observational work of Li & Carbone (2012) argues that the PA is responsible for the convective rainfall excitation over the western Pacific tropical warm pool on daily scales, and the work by Ma et al. (2020) successfully describes the fast atmospheric response to the cold wakes generated by tropical cyclones in terms of secondary circulations controlled by the PA mechanism. Thus, there is evidence that both mechanisms contribute to the atmospheric response over a large range of spatio-temporal scales.

Most of the idealized model studies, as those by Skyllingstad et al. (2007); Kilpatrick et al. (2014); Spall (2007), and Wenegrat & Arthur (2018), show that the DMM is more important than the PA over small frontal structures and short time scales. However, a few works stand out. For example, Skyllingstad et al. (2019) demonstrate that the PA is the dominating mechanism in the convective rainfall excitation on daily scales in the tropical ocean, as observed by Li & Carbone (2012). Lambaerts et al. (2013) show that the PA is important over hourly time scales, especially in low background wind conditions. Also Foussard et al. (2019) argue that the PA-mediated fast atmospheric response has been overlooked in the past because the disruptive effect of the advection on the standard metrics has not been properly considered, as described below.

To measure the action of the PA mechanism, it is common practice to calculate the correlation coefficient or the slope of the linear fit of the binned distributions of the SST Laplacian and the surface wind (or wind stress) divergence (Minobe et al., 2008; Lambaerts et al., 2013; Meroni et al., 2020). Foussard et al. (2019) highlight the shortcomings of considering these two variables, because the advection might shift the atmospheric field and the co-location between the SST forcing and the corresponding MABL response might be lost. To overcome this issue, they propose to use the correlation between the air temperature Laplacian, rather than SST Laplacian, and the wind divergence, showing that the PA is as important as (or even more than) the DMM in some environmental conditions. However, air temperature is not an easy variable to observe and, thus, this approach cannot be followed when analyzing satellite observations.

Goal of this study is to define and test some new metrics to detect the PA mechanism that are robust even in the presence of background wind. In particular, these metrics are based on wind field and SST only, that can be retrieved from satellite measurements and for which there are long-term climate data records (Merchant et al., 2019; Verhoef et al., 2017, e.g.). To do so, we exploit a set of high-resolution realistic numerical simulations that have different SST forcing fields. Other than the reference high-resolution experiment, there are two runs with enhanced and reduced SST gradients, and a set of runs with different levels of smoothing of the SST field.

Section 2 describes the numerical model and the performed experiments, section 3 formally introduces the methods and the new metrics. Section 4 describes the results in terms of skills of the metrics, with a focus on the dependence on the strength of the SST gradients and the spatial scales involved. Section 5 discusses and interprets the results and shows an example of application of the new metrics on seasonal statistics over the Mediterranean Sea. Conclusions are drawn in section 6.

2 Numerical model and experiments

We exploit a set of high-resolution realistic simulations with artificially modified SST forcing fields performed with the Weather Research and Forecasting (WRF) model

Table 1. Summary of the SST Forcing Fields of the Various Simulations. Symbols are defined in the main text.

Name	SST forcing field
CNTRL	$SST_0(x,y) = \overline{SST} + SST'(x,y)$
UNIF	$\overline{SST}$
ANML_HALF	$\overline{SST} + 0.5 \cdot SST'(x,y)$
ANML_DOUBLE	$\overline{SST} + 2 \cdot SST'(x,y)$
SM1	$G_1 * SST_0(x,y)$
SM2	$G_2 * SST_0(x,y)$
SM4	$G_4 * SST_0(x,y)$
SM8	$G_8 * SST_0(x,y)$
SM16	$G_{16} * SST_0(x,y)$

SST = sea surface temperature.

V3.6.1 (Skamarock et al., 2008). We use its Advanced Research core that solves the fully compressible non-hydrostatic Euler equations. The model exploits an Arakawa-C grid in the horizontal and mass-based terrain following vertical coordinates. The grid step is 1.4 km and there are 84 vertical levels. More details on the numerical setup, the numerical schemes and the boundary conditions used can be found in Meroni, Parodi, & Pasquero (2018). All simulations are initialized at 0000UTC on the 6^{th} of October 2014 and last for four days only. This enables to run a high number of experiments with a low computational cost. In the present work, only the first output of the simulations, taken at 0100UTC on the 6^{th} of October 2014, is considered in the analysis, for reasons discussed in the next section.

The reference simulation is named CNTRL and is forced with a high-resolution SST field, denoted with $SST_0(x,y)$, obtained from a realistic eddy-resolving ocean simulation integrated with ROMS (Regional Ocean Modeling System) in its CROCO (Coastal and Regional Ocean COmmunity model) version (Penven et al., 2006; Debreu et al., 2012), as described in Meroni, Renault, et al. (2018). The UNIF experiment is run with a uniform SST field, equal to the spatial mean of the CNTRL SST, indicated as $\overline{SST}$. By taking the difference between the CNTRL and the UNIF SST field, one obtains the SST anomaly, $SST'(x,y) = SST_0(x,y) - \overline{SST}$, which can be increased or reduced to modify the SST gradients. By multiplying the anomaly by a coefficient α and summing back the UNIF SST value, then, one gets an SST field with enhanced or reduced SST gradients but with the same mean value as the CNTRL run. The SST fields of the ANML_HALF and ANML_DOUBLE simulations are obtained in this way (with $\alpha = 0.5$ and $\alpha = 2$ respectively) to get halved and doubled SST gradients. Note that the gradients are modified just by changing the SST magnitude, and not its spatial scales. The other set of simulations considered, instead, has an increasing degree of smoothing of the SST field starting from the CNTRL case. A Gaussian filter, valid over sea points only, is used to smooth the SST field with a standard bi-dimensional convolution operation, indicated with $*$. Note that this filter is set to zero after three spatial standard deviations. It is named G_β and, correspondingly, the experiments are named SMβ, with $\beta \in [1, 2, 4, 8, 16]$ indicating the standard deviation of the Gaussian filter in km. The names of the simulations considered are summarized in Table 1 and all the details of the SST forcing fields, with their appropriate analytical definitions, are thoroughly described in Meroni, Parodi, & Pasquero (2018).

3 Methods

Thanks to the availability of the UNIF simulation, the effects of the spatial SST structures on the atmospheric dynamics can be directly evaluated. This is accomplished by taking the instantaneous difference of the relevant fields from the simulation of interest with respect to the same field from the UNIF simulation. We denote this operation with the Δ symbol, so that the ΔSST of the CNTRL run is

$$\Delta\mathrm{SST}_{\mathrm{CNTRL}}(x,y) = \mathrm{SST}_{\mathrm{CNTRL}}(x,y) - \mathrm{SST}_{\mathrm{UNIF}}(x,y) \tag{1}$$

In particular, we consider the first hour of the simulations, so that the trajectories of the UNIF run and of the other runs have not diverged too much because of the chaotic nature of the equations and because of different wave propagation features (for example in the surface pressure field). To directly evaluate the PA mechanism in terms of pressure response due to the SST spatial structure we compute the Pearson ρ spatial correlation coefficient between ΔSLP (sea level pressure) and ΔSST from various simulations.

As a benchmark, we compute the standard metrics used in the literature to measure the action of the PA mechanism (Minobe et al., 2008; Foussard et al., 2019; Meroni, Parodi, & Pasquero, 2018): the spatial correlation between wind divergence δ and SST Laplacian Λ, written in spherical coordinates as

$$\delta = \frac{1}{R\cos\theta}\frac{\partial u}{\partial \varphi} + \frac{1}{R\cos\theta}\frac{\partial}{\partial\theta}(v\cos\theta), \tag{2}$$

$$\Lambda = \frac{1}{R^2\cos^2\theta}\frac{\partial^2 \mathrm{SST}}{\partial\varphi^2} + \frac{1}{R^2\cos^2\theta}\frac{\partial}{\partial\theta}\left(\frac{\partial \mathrm{SST}}{\partial\theta}\cos\theta\right). \tag{3}$$

The spherical coordinates $\{\varphi,\theta\}$ are defined over a sphere of radius $R = 6371$ km, with φ denoting the longitude and θ denoting the latitude.

In order to introduce the new metrics, we define a local Cartesian frame of reference based on the background wind field. In particular, the wind components (u,v) can be written as the sum of a large-scale wind (U,V) and an anomaly (u',v'), so that

$$u = U + u'; \quad v = V + v' \tag{4}$$

in the standard local Cartesian frame of reference $\{x,y\}$, with x increasing eastward and y increasing northward. Another instantaneous local Cartesian frame of reference $\{r,s\}$ can be defined according to the large scale wind vector (U,V), whose precise definition is given later, with r being the along-wind direction and s the across-wind direction (positive at 90°counter-clockwise with respect to r), as sketched in figure 1. With such a definition, a vector (a_x,a_y) in the $\{x,y\}$ frame is readily transformed in the $\{r,s\}$ frame with a standard rotation, namely

$$a_r = a_x\cos\phi + a_y\sin\phi; \quad a_s = -a_x\sin\phi + a_y\cos\phi, \tag{5}$$

with $\cos\phi = U/|\boldsymbol{U}|$ and $\sin\phi = V/|\boldsymbol{U}|$. In particular, the wind field in the new frame of reference is

$$\dot{r} = u\cos\phi + v\sin\phi; \quad \dot{s} = -u\sin\phi + v\cos\phi, \tag{6}$$

and, by definition, can be decomposed as

$$\dot{r} = |\boldsymbol{U}| + \dot{r}'; \quad \dot{s} = \dot{s}'. \tag{7}$$

With the same approach, by projecting the gradient of a given quantity ψ, $\boldsymbol{\nabla}\psi$, onto the new directions $\{r,s\}$, one gets the derivatives with respect to r and s as

$$\frac{\partial\psi}{\partial r} = \hat{\boldsymbol{r}}\cdot\boldsymbol{\nabla}\psi; \quad \frac{\partial\psi}{\partial s} = \hat{\boldsymbol{s}}\cdot\boldsymbol{\nabla}\psi, \tag{8}$$

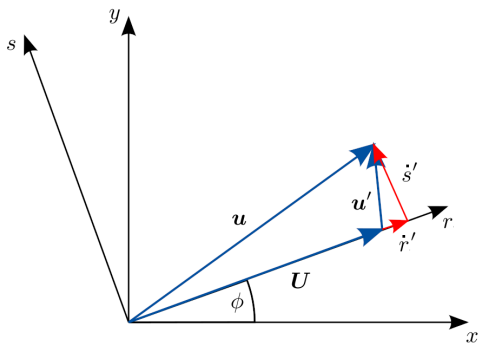

Figure 1. Schematic of the rotated local Cartesian frame of reference $\{r, s\}$ defined according to the large-scale wind vector $\boldsymbol{U}$. The wind anomaly components in the rotated frame of reference $(\dot{r}', \dot{s}')$ are shown with the small red arrows. All symbols are defined in the main text.

with $\hat{\boldsymbol{r}}$ and $\hat{\boldsymbol{s}}$ being the unit vectors of the new coordinates. In particular, using $\{\varphi, \theta\}$, the local rotation with respect to the large-scale wind is the same as for the local standard Cartesian frame of reference $\{x, y\}$ as in equation (5) and, thus,

$$\frac{\partial \psi}{\partial r} = \frac{\cos\phi}{R\cos\theta}\frac{\partial \psi}{\partial \varphi} + \frac{\sin\phi}{R}\frac{\partial \psi}{\partial \theta}; \tag{9}$$

$$\frac{\partial \psi}{\partial s} = \frac{-\sin\phi}{R\cos\theta}\frac{\partial \psi}{\partial \varphi} + \frac{\cos\phi}{R}\frac{\partial \psi}{\partial \theta}. \tag{10}$$

In the rotated frame of reference two new quantities are defined: the across-wind divergence

$$\delta_s = \frac{\partial \dot{s}'}{\partial s} = \frac{\partial \dot{s}}{\partial s} \tag{11}$$

and the across-wind SST Laplacian

$$\Lambda_s = \frac{\partial^2 \mathrm{SST}}{\partial s^2}. \tag{12}$$

In a similar way, the along-wind divergence

$$\delta_r = \frac{\partial \dot{r}'}{\partial r} \tag{13}$$

and the along-wind SST Laplacian

$$\Lambda_r = \frac{\partial^2 \mathrm{SST}}{\partial r^2} \tag{14}$$

can be introduced. Note that in the along-wind divergence δ_r the large scale wind is removed because, by definition, it is a smooth field and does not respond to the small-scale SST structures, which are the main focus of the present work.

The strength of using this rotated frame of reference to detect the PA mechanism comes from the fact that pressure is a scalar and produces gradients and, possibly, a dynamical response in all directions. In fact, by looking at the across-wind direction, it is possible to remove the effects of the large-scale advection, which are known to mask the PA signal (Foussard et al., 2019; Lambaerts et al., 2013).

Another approach to reduce the effect of advection is to stretch the coordinates $\{x, y\}$ along the direction of the large-scale wind using the following transformation

$$x_\star = \frac{x}{|U|}; \quad y_\star = \frac{y}{|V|}. \tag{15}$$

This means that $\{x_\star, y_\star\}$ are time coordinates and can be used to introduce the stretched wind divergence $\delta_\star$ and the stretched divergence of the SST gradient, which we call stretched SST Laplacian $\Lambda_\star$. In spherical coordinates they are written as

$$\delta_\star = \frac{|U|}{R\cos\theta}\frac{\partial u}{\partial \varphi} + \frac{|V|}{R\cos\theta}\frac{\partial}{\partial\theta}(v\cos\theta), \tag{16}$$

$$\Lambda_\star = \frac{|U|}{R^2\cos^2\theta}\frac{\partial^2 \mathrm{SST}}{\partial\varphi^2} + \frac{|V|}{R^2\cos^2\theta}\frac{\partial}{\partial\theta}\left(\frac{\partial \mathrm{SST}}{\partial\theta}\cos\theta\right). \tag{17}$$

Alternatively, to focus on the small-scale response, one can remove the large scale wind and compute the divergence of the wind anomaly (u', v'), namely

$$\delta' = \frac{1}{R\cos\theta}\frac{\partial u'}{\partial \varphi} + \frac{1}{R\cos\theta}\frac{\partial}{\partial\theta}(v'\cos\theta), \tag{18}$$

which we call wind divergence prime. This is equivalent to the sum of the across-wind and the along-wind divergence defined above

$$\delta' = \delta_r + \delta_s, \tag{19}$$

as the horizontal divergence does not depend on the local rotation of the frame of reference. As for the along-wind divergence δ_r introduced above, this metrics does not consider the large-scale wind divergence, which is a relatively smooth field and should be independent of the small-scale spatial SST features.

In what follows, the large-scale wind is computed using a bi-dimensional Gaussian filter on the valid points over the sea with a standard deviation of 10 grid steps (roughly 14 km), unless stated otherwise. A sensitivity to this value is discussed in the next section. A coastal strip of roughly 20 km is removed from the analysis, to avoid including some features that develop in the first few hours of the simulation with numerical waves propagating from the coastlines over the sea.

Two kinds of spatial correlation coefficients are considered: the Pearson ρ and the Spearman r, which is the Pearson correlation coefficient calculated using the ranking of the values, instead of the values themselves (Press et al., 1992). While the Pearson ρ coefficient measures the linearity of the relationship between the two variables under study, the Spearman r measures how much their relationship is monotonic. The statistical significance of the Spearman r coefficient is assessed with a Student-t test (Press et al., 1992).

In the literature, binned distributions have been used to measure the strength of the air-sea coupling, by computing their slope to get the so-called coupling coefficients (Renault et al., 2019; Small et al., 2008; Chelton & Xie, 2010, e.g.). As the least-square estimate of the linear trend is not robust with respect to the presence of outliers, the extreme values in the binned distribution can control the value of the coupling coefficient, especially when instantaneous data are considered. To avoid this, we introduce the percentile distribution, which is a standard binned distribution whose bins are not regular in terms of values of the control variable, but are regular in terms of number of points per bin, as in Desbiolles et al. (2021). In particular, we compute the mean value and standard error of the dependent variable (y axis) conditioned to the percentile bins of the control variable (x axis). All figures and coefficients shown in this work are computed using 20 bins containing 5% of the points each. The results were tested not to be sensitive to this choice by considering bins with 2% and 10% of the points (not shown).

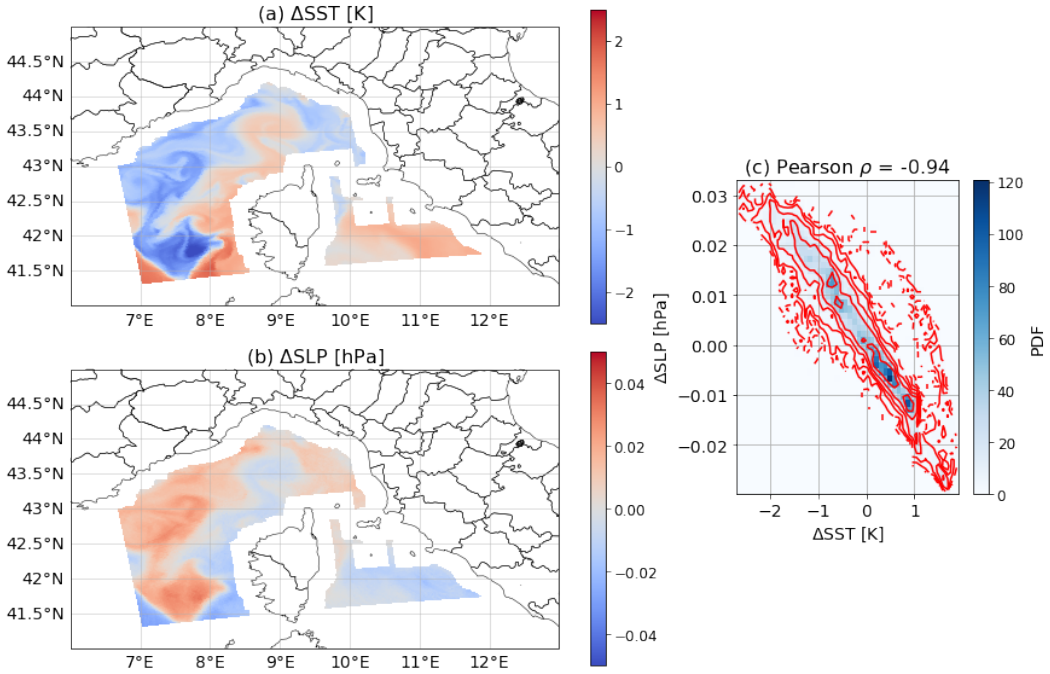

Figure 2. Instantaneous maps of (a) ΔSST and (b) ΔSLP from the CNTRL simulation at 0100UTC on the 6th of October 2014. (c) Bi-dimensional distribution of the same variables shown with colors as a normalized probability density function (PDF). The red lines indicate the contours of the logarithm of the same PDF.

The spatial correlation coefficients are computed either directly on the pointwise values of the relevant fields or on their percentile distributions. By computing the correlation coefficient on the percentile distribution one can assess whether the PA mechanism is acting or not, while with the coupling coefficient one can measure the strength of the atmospheric response.

4 Results

By looking at the correlation between ΔSST and ΔSLP from the CNTRL simulation we can directly evaluate the pressure response to the presence of small-scale SST features. Having a small-scale SST field introduces small SLP anomalies that are highly correlated to the SST anomalies, as shown in figure 2. In particular, a strong correspondence between the ΔSST and ΔSLP fields is visible in the maps of panels (a) and (b). This is confirmed by the high (in absolute value) and statistically significant (>99%) spatial Pearson $\rho = -0.94$ obtained between the same two fields. Thus, this proves that the PA mechanism is efficiently acting on hourly scales over fine SST structures at mid-latitudes, as in the present experiments.

However, the spatial correlation between the SST Laplacian and the wind divergence taken from the same instant of the CNTRL simulation is very low. The fact that the two fields considered are not correlated is visible both from their bi-dimensional distribution and from their percentile distribution, both shown in figure 3. In particular, from the bi-dimensional distribution in panel (a) it is clear how the wind divergence is unrelated to the SST Laplacian, especially for very low values of SST Laplacian. The two fields have a very low Pearson ρ, which indicates that the wind divergence variance

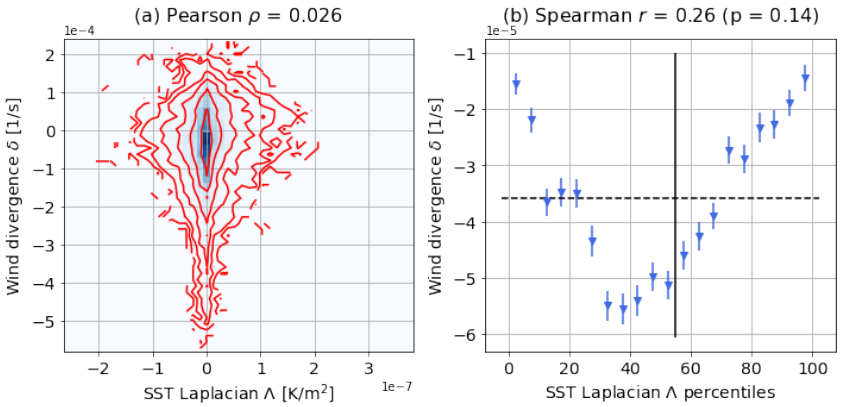

Figure 3. (a) Bi-dimensional distribution and (b) percentile distribution of the SST Laplacian and the wind divergence from the CNTRL experiment. In (b) the error bars show the standard error of the bins, the vertical line indicates where the SST Laplacian changes sign and the horizontal dashed line the mean value of the wind divergence.

explained by the linear model as a function of the SST Laplacian is very low ($\rho^2 \sim 0.1\%$). This is physically related to the fact that the atmospheric dynamics is controlled by many processes that have nothing to do with the SST field. From the percentile distribution of panel (b) one can see that there is not a monotonic increasing trend in the wind divergence response for increasing SST Laplacian, indicating that, in this case, the standard metric used to detect the action of the PA mechanism is failing. This is confirmed by the low and non-significant (at the 99% level) Spearman $r = 0.26$ coefficient calculated on the percentile distribution.

The fact that the PA is acting over hourly time scales in a midlatitudes setup, as shown by the Pearson ρ between the ΔSLP and ΔSST fields, is in agreement with the results of Lambaerts et al. (2013). In their work, they are able to show it by computing the standard metrics (correlation coefficient between the vertical wind velocity, closely related to the horizontal wind divergence, and the SST Laplacian) in some idealized numerical simulation with absent or very weak (1 m s^{-1}) background wind. The fact that here the correlation between the standard variables is low can be explained by the presence of a non-zero background wind (whose histogram is shown in figure 4). It ranges from 0 to 5 m s^{-1}, with a mean value of 3 m s^{-1} over the sea in the instant considered. In agreement with the arguments presented by Foussard et al. (2019), the presence of a non-zero mean wind breaks the spatial correlation between SST Laplacian and wind divergence.

Consider, now, figure 5, that shows the bi-dimensional distributions (left column) and the percentile distributions (right column) of the new metrics. The advantages of considering the across-wind direction to detect the atmospheric response mediated by the PA mechanism clearly emerge from panels (a) and (b). In fact, the bi-dimensional distribution of the across-wind divergence and the across-wind SST Laplacian, panel (a), appears to be more symmetric with respect to the origin and shows a slight tilt far from the zero across-wind SST Laplacian value. The Person $\rho = 0.038$ is still low and not significant at the 99% percent level. The tilt visible in the bi-dimensional distribution, that corresponds to increasing across-wind divergence for increasing across-wind SST Laplacian, becomes more evident in the percentile distribution in panel (b). This is found to have a high Spearman $r = 0.85$, statistically significant at the 99% level, indicating that the trend is truly positive. It is interesting to highlight that for very negative (positive)

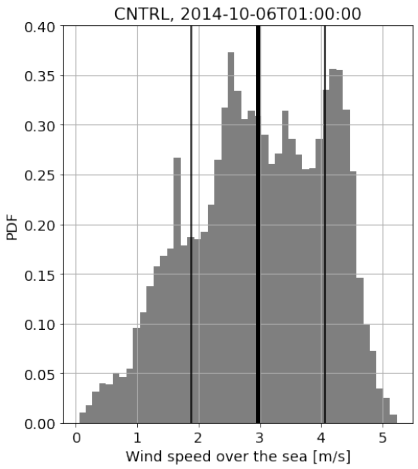

Figure 4. Histogram of the wind speed over the sea from the CNTRL experiment at the instant considered. Vertical lines indicate the mean value (thin line in the middle) and the mean ± one standard deviation.

across-wind SST Laplacian, across-wind surface wind convergence (divergence) is found, indicated by the blue downward (red upward) triangles, in agreement with the action of the physical mechanism.

The use of the stretched coordinates, as panels (c) and (d) show, does not improve the skills of the correlation coefficient in detecting the action of the PA, neither in terms of Pearson ρ nor in terms of Spearman r of the percentile distribution. Moreover, no divergence is ever observed in the percentile distribution values, not even at the highest percentiles. This is due to the presence of a large-scale negative divergence component, which also emerges in the wind divergence field shown in figure 3, that causes the mean value to be negative. This is confirmed by the distributions of the wind divergence prime field, shown in panels (e) and (f). In fact, it appears that the mean wind divergence prime ($\sim 0.25{\times}10^{-5}$ s^{-1}) is an order of magnitude closer to zero than the mean wind divergence ($\sim\ -3.5 \times 10^{-5}$ s^{-1}), indicating that the negative bias of the wind divergence and the stretched wind divergence fields is really due to the large-scale. Also using the wind divergence prime (i.e. removing the large-scale wind) in the calculation of the correlation coefficients is not enough to highlight the small-scale atmospheric response controlled by the PA mechanism. In fact, both the Pearson $\rho = 0.028$ and the Spearman $r = 0.43$ and relatively low and not significant at the 99% level.

Figure 6 shows the maps of (a) the across-wind SST Laplacian and of (b) the difference between the across-wind divergence of the CNTRL case and of the UNIF case, i.e. the $\Delta\delta_s$ field. Note that the large-scale wind from the CNTRL simulation has been used to compute $\Delta\delta_s$, also for the UNIF term. These maps confirm by visual inspection that there is an imprint in the small-scale wind divergence thanks to the PA mechanism that acts over the small-scale SST features.

4.1 Dependence on the strength of the SST gradients

Consider the set of experiments that includes ANML_HALF, CNTRL and ANML_DOUBLE. By definition of their forcing SST fields, they all have the same spatial mean SST value (equal to the uniform SST used in the UNIF case), with unchanged spatial scales and the SST gradients increasing by a factor of 2. By directly computing the spatial correlation between the ΔSLP and ΔSST fields, we can state that the PA is responsible for

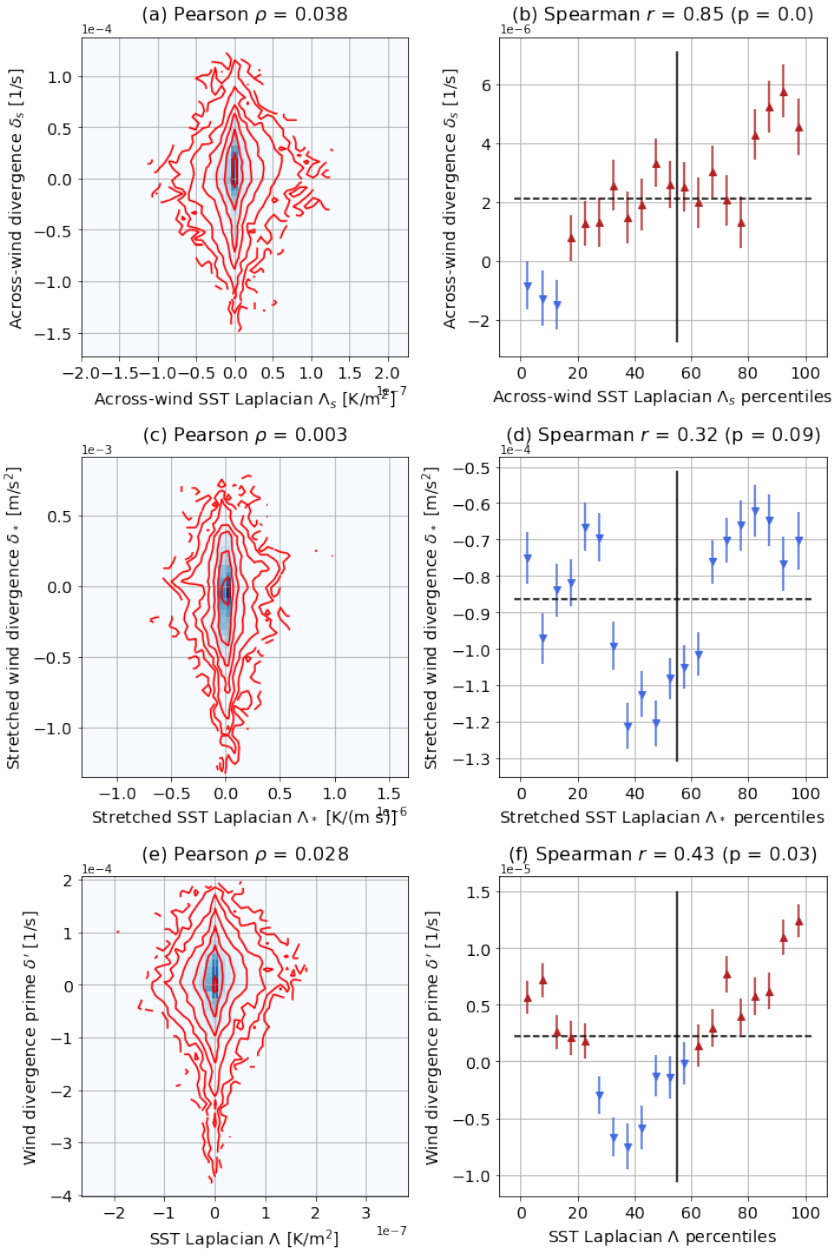

Figure 5. Bi-dimensional (left column) and percentile (right column) distributions of: (a)-(b) across-wind SST Laplacian Λ_s and across-wind divergence δ_s; (c)-(d) stretched SST Laplacian $\Lambda_\star$ and stretched wind divergence $\delta_\star$; (e)-(f) SST Laplacian Λ and wind divergence prime δ'. In (a), (c), (e) the blue shades indicate the PDF and the red lines indicate the log of the PDF. In (b), (d), (f) the horizontal lines denote the sample average of the variable displayed on the y axis and the vertical lines indicate where the variable on the x axis changes sign.

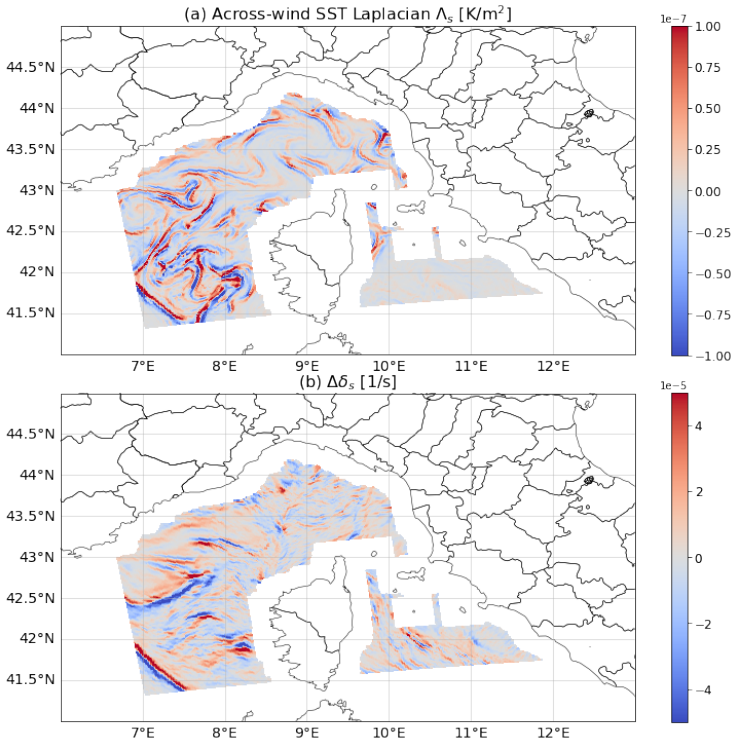

Figure 6. Maps of (a) across-wind SST Laplacian Λ_s from the CNTRL case and (b) $\Delta\delta_s$, the difference of the across-wind divergence from the CNTRL case and the UNIF case, with the large-scale wind used to defined the rotated frame of reference $\{r, s\}$ coming from the CNTRL simulation.

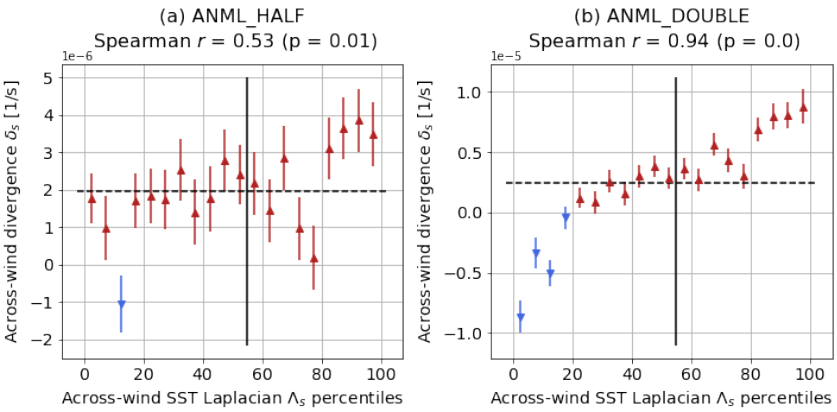

Figure 7. Percentile distributions of across-wind SST Laplacian and across-wind divergence from the ANML_HALF (a) and ANML_DOUBLE (b) simulations. The vertical lines indicate the change of sign of the across-wind SST Laplacian and the horizontal dashed lines indicate the mean across-wind divergence.

the atmospheric adjustment irrespective of the strength of the SST gradients, even if they are halved with respect to the CNTRL case. This is proven by the very high (in absolute value) and statistically significant Pearson ρ (at the 99% level) calculated in all three cases and visible in figure S1 of the Supporting Information.

Figure 7 shows the percentile distributions of the across-wind variables, Λ_s and δ_s for the ANML_HALF and ANML_DOUBLE runs. The new metrics based on the across-wind variables is found to be able to detect a significant correlation (in terms of Spearman r) in both cases. In agreement with the previous results from the CNTRL simulation only, and with the physical understanding of the mechanism, the results from this set of simulations indicate that the stronger the SST spatial variability (and, thus, the first and second spatial derivatives of the SST fields), the stronger the impact on the surface wind dynamics. This implies, then, that the skills of the correlation coefficients in detecting the action of the PA mechanism increase with the stronger SST variability.

In the Supporting Information, figures S2 and S3 show the bi-dimensional and the percentile distributions of the standard variables, SST Laplacian Λ and wind divergence δ, and of the across-wind variables, Λ_s and δ_s, respectively, for the ANML_HALF, CNTRL and ANML_DOUBLE simulations. It appears that the correlations between SST Laplacian and wind divergence are low and non-significant, whereas the correlations between across-wind variables are so. Thus, fine-scale strong SST variations (on the same spatial scale over which the wind dynamics is resolved) have an imprint in the surface wind divergence field on short time scales. By reducing the masking effect of the advection, in particular by looking at the across-wind direction, the PA action can be successfully detected, which is not the case if the standard variables (SST Laplacian and wind divergence) are used. Moreover, the fact that the Spearman r increases going from ANML_HALF to ANML_DOUBLE suggests that the presence of stronger SST variability makes this metrics more efficient. More on this aspect is developed in the next section.

4.2 Spatial scale of the response

Let us focus on the characteristic length scales of the atmospheric response. In the first place, considering the CNTRL simulation, we can test two things: (1) the skills of the standard metrics (based on Λ and δ) as a function of the standard deviation σ of a

Gaussian filter used to smooth the SST Laplacian and wind divergence fields themselves, and (2) the skills of the across-wind metrics (based on Λ_s and δ_s) as a function of the standard deviation σ used to define the large-scale background wind field.

Panel (a) of figure 8 shows the Spearman r coefficients between the percentile distributions of the smoothed SST Laplacian and the smoothed wind divergence (blue circles), and of the across-wind SST Laplacian and the across-wind divergence (orange triangles) taken from the CNTRL simulation, as a function of the σ of the Gaussian filters mentioned above. In particular, large and small markers indicate Spearman r that are statistically significant at the 99% and 95% level, respectively. The Spearman r between the smoothed standard variables (blue circles) shows that for a very local smoothing (small σ), the correlation is relatively low, $\sim$0.4, while a peak in the correlation is reached with σ between 25 and 30 km. This is interpreted to be due to a reduced masking effect of the advection when the fields are smoother, as discussed in the next section. In the same panel, the across-wind variables (orange triangles) clearly show a high and significant correlation up to $\sigma \sim 25$ km. With σ between 25 km and 40 km the correlation drops and after 40 km it is no longer significant at the 99% level. In the limit of very large σ, the correlation is expected to be similar to the value of the non-filtered standard metric (correlation between the SST Laplacian and the wind divergence), as a uniform background wind is used to compute the across-wind derivatives and no information on the local structure of the flow is retained. This confirms that the metrics based on the across-wind variables is able to detect the PA signal for $\sigma < 25$ km.

We now exploit the set of simulations with a smoothed SST field, the SMβ set of experiments, to test the skills of new metrics in detecting the PA when the SST gradients get weaker both because the SST variability decreases and because their spatial scales increase. Note that the standard deviation of the filter applied to the SST forcing β is completely independent from the standard deviation of the filters applied to the diagnostic fields σ. We verify that the direct atmospheric response in terms of pressure, measured by the Pearson ρ correlation between ΔSLP and ΔSST is strong and significant in all SMβ cases. It is found that the correlation is always lower than -0.91. Thus, despite the SST first and second derivatives get weaker because of the spatial smoothing, the presence of a non-uniform SST in the lower boundary introduces a direct atmospheric response in terms of surface pressure. The maps of ΔSLP and ΔSST also confirm the strong correspondence of the two fields (not shown).

However, for larger and larger spatial scales of the SST structures (corresponding to high β in the SMβ simulations), the scales of the SST-induced pressure gradients also increase. This means that, at fine scales, the SST structure does not produce any pressure gradient that can alter the wind field, and, thus, the fine-scale wind variability cannot be constrained by the SST. This can be tested by changing the standard deviation of the Gaussian filter used to calculate the background wind speed σ and considering all simulations of the SMβ set, as described in what follows.

Note that in the definition of the across-wind divergence δ_s and the primed wind divergence δ' the background wind field is removed. Thus, considering these variables instead of the wind divergence δ is a form of high-pass filter whose cutoff length is determined by σ itself. The larger the σ, the smoother the background wind field, but the wind divergence fields always have a small-scale component. So far, the background wind Gaussian filter has been defined with a standard deviation σ of 10 grid points (equivalent to 14 km), but its values can be used to select the scales of the atmospheric response of interest in the δ_s and δ' fields.

Considering smoother SST forcing fields, as shown in panels (b)-(f) for the SMβ experiments, a consistent behavior of the smoothed standard variables (blue circles) emerges. In fact, it is always found that a smoothing with a σ of 20-30 km is needed to reduce the advection effect and get the peak in correlation suggesting that the SST forcing at these

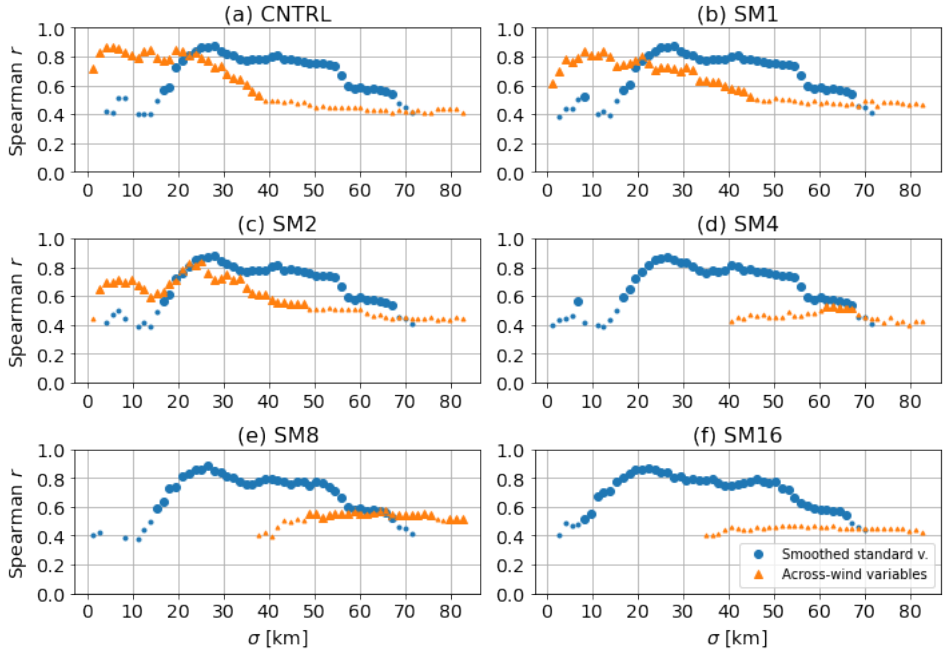

Figure 8. Spearman r coefficients calculated on the percentile distributions of the across-wind variables (orange triangles) and of the smoothed standard variables (SST Laplacian and wind divergence, blue circles). The coefficients are shown as a function of the standard deviation σ of the Gaussian filter used either to determine the background wind for the across-wind variables shown with the orange triangles or to spatially smooth the SST Laplacian and the wind divergence shown with the blue circles. The titles of the panel show the names of the simulations considered. Small and large symbols show the coefficients significant at the 95% and 99% level, respectively.

scales is detected by the atmospheric dynamical response. In terms of across-wind variables (orange triangles), instead, it emerges that when the forcing SST field does not have any small-scale feature (starting from SM4, panel (d), and for higher β), the wind field is not constrained by the SST and the correlation is not significant for $\sigma < 20-30$ km. For higher σ, instead, the Spearman r of the across-wind variable tends to the Spearman r of the non-smoothed standard variables (SST Laplacian and wind divergence), as previously discussed. This confirms that the metrics based on the across-wind variables does not detect any small-scale atmospheric response in the case where no small-scale SST forcing is present, which is important to show for the definition of a new metrics.

Finally, the Spearman r correlation between the percentile distributions of the stretched SST Laplacian and the stretched wind divergence has a very weak dependence on the σ used to determine the background wind field for both the CNTRL and all the SMβ runs (not shown). This happens because in the calculation of the stretched variables the large-scale wind is not removed and there is no high-pass filter behavior. For all cases, then, the correlation is never significant at the 99% level. Instead, we do not show the Spearman r correlation between the SST Laplacian and the wind divergence prime δ', because its behavior as a function of σ is similar to the across-wind variables one, with generally lower correlation values.

5 Discussion

To interpret the results further, we can consider the spatial scale over which the PA is estimated to produce a response in the wind field. In the literature, the characteristic time scale of the PA mechanism is written as h^2/K_T, where h is the MABL height and K_T is the thermal eddy turbulent coefficient (Small et al., 2008). Physically, this corresponds to the time required for a non-negligible pressure anomaly to develop, which is controlled by the temperature mixing in the MABL. By looking at the CNTRL simulation, the MABL height is between 300 and 1400 m, whereas a typical mid-latitude value for K_T is 15 m^2 s^{-1} (Redelsperger et al., 2019). By multiplying the PA time scale by the typical wind speed U_0, one gets the length scale over which PA produces a wind response (Small et al., 2008). In particular, using the mean wind speed of $U_0 \sim 3$ m s^{-1} of the instant of the simulation considered (see figure 4), the PA length scale $L_p \sim U_0 h^2/K_T$ is in the range between 15 and 360 km. It is interesting to notice that the σ of the filter that maximizes the Spearman r between the smoothed SST Laplacian and the smoothed wind divergence, which is around 30 km, falls in this range. In particular, as the extent of the Gaussian filter is actually 3 times its standard deviation, we can consider that the length scale of the structures that maximize the SST Laplacian and wind divergence correlation is roughly 100 km, which is very close to the mean value of $L_p \sim 120$ km. This suggests that the masking effect of the advection on the spatial correlation between SST Laplacian and wind divergence is reduced when some smoothing is performed on the wind field and when the scales of the forcing SST are of the same order as the PA length scale.

In other words, the PA-mediated secondary circulation develops in response to the underlying SST structures on a length scale L_p, which, in the direction of the wind, is large compared to the typical SST structures. Thus, as the response of the air moving with the flow is integrated over the small scale SST variability, it is only sensitive to the smoother and larger scale thermal features. In the across-wind direction, the advection U_0 tends to zero and, thus, the length scale for the PA response, L_p, tends to zero as well. For this reason, the spatial response mediated by the PA can be detected over very small scales by the newly introduced metrics, as previously demonstrated.

None of the two other metrics is found to be skillful. In fact, the use of the coordinate stretching does not produce any positive effects on the correlations, because there is no selection of the small scales (accomplished in the other cases with the subtraction of the background wind). By removing the large-scale wind before computing the wind divergence (as done with the δ' field), then, one gets a modest improvement with respect to the full wind divergence field. This is explained by the presence of the effects of the large-scale advection, which keeps the skills of this metrics lower than the across-wind one. This corresponds to the fact that the integral PA-mediated atmospheric response is realized over relatively large L_p scales.

Finally, we show that the new metrics based on the across-wind variables also works on some high-resolution satellite data. To do so, we consider the daily L4 ESA CCI (European Space Agency Climate Change Initiative) SST analysis product v2.1 (Merchant et al., 2019; Good et al., 2019) and the instantaneous L2 coastal METOP-A ASCAT (METeorological OPerational satellite-A Advanced SCATterometer) wind field CDR (Climate Data Record) product (Verhoef et al., 2017). The ESA CCI SST analysis is given on a regular 0.05° grid and the METOP-A ASCAT wind on its irregular along-track grid at 12.5 km nominal resolution.

Considering all the wind swaths within the spring season (from the 1st of March to the 31st of May 2010) over the Mediterranean Sea, the seasonal percentile distributions for the standard metrics (SST Laplacian and wind divergence) and the across-wind variables can be computed (see figure 9). It appears that a different response is detected according to the variables considered. In particular, no relationship between the wind divergence and the SST Laplacian is detected, in agreement with previous studies such

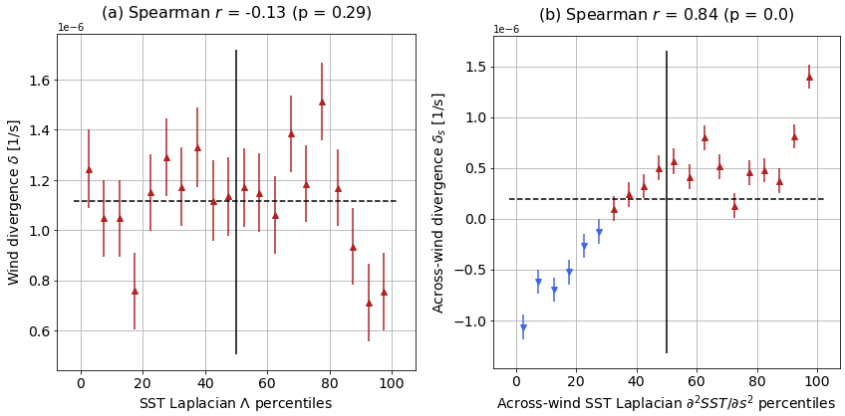

Figure 9. Spring percentile distributions (mean and standard error for each bin) calculated over the Mediterranean Sea for (a) SST Laplacian Λ and wind divergence δ, and (b) across-wind Laplacian $\Lambda_s = \partial \mathrm{SST}/\partial s$ and across-wind divergence δ_s. The L4 ESA CCI SST analysis product and the L2 METOP-A ASCAT CDR wind field product are used. The horizontal dashed lines denote the mean value of the variable shown on the y axis and the vertical solid lines indicate the percentile where the variable shown on the x axis changes sign.

as Meroni et al. (2020) and Desbiolles et al. (2021). However, a significant Spearman r correlation is found between the across-wind variables, suggesting that the PA is actually at play, as found from the numerical simulations presented in this work. Thus, concluding that the PA mechanism does not control the atmospheric wind response over the Mediterranean Sea might be incorrect just because the signal is masked by advection, as discussed in the previous sections. A full characterization of the wind response using these data goes beyond the scope of the present work and will be considered in a future work. Here, we can state that the newly defined across-wind metrics is able to detect a PA-mediated signal even in high resolution remote sensing observational products.

6 Conclusions

The PA mechanism is mostly known in the literature to produce a wind divergence response over large SST structures and relatively long scales, namely seasonal and annual (Minobe et al., 2008; Takatama et al., 2015). Evidence of its control on the wind divergence over fine-scale SST structures and short time scales has been detected either in very low or absent background wind environments (Lambaerts et al., 2013), or exploiting correlation coefficients between wind divergence and air temperature (Foussard et al., 2019), which is not easy to observe from satellites. Advection has been proposed to be the main responsible for the breaking of the correlation between SST Laplacian and wind divergence (Foussard et al., 2019), which is one of the standard PA metrics (Minobe et al., 2008; Small et al., 2008).

In this work, we introduce and test three new metrics to detect the fast action of the PA exploiting SST and wind field data, only. The skills of the new metrics are evaluated using a set of high-resolution realistic numerical atmospheric simulations with appropriately modified SST forcing fields. In particular, the presence of a simulation with a uniform SST field enables to directly look at the effects of the SST spatial structures on the MABL dynamics. Among the proposed metrics, only the one based on the correlation between the across-wind SST Laplacian and the across-wind divergence, so that the masking effect of the large-scale wind advection is reduced, is able to detect the PA-

mediated atmospheric response. This approach exploits the fact that pressure is a scalar and it can produce gradients in all directions. A significant Spearman r correlation between the across-wind SST Laplacian and the across-wind divergence is found when the SST forcing field has small-scale spatial structures, whereas no correlation is detected when the forcing SST field is smoothed. This is in line with the physical interpretation of the characteristic length scale of the PA-mediated response, $L_p \sim U_0 h^2 / K_T$, which is large in the along-wind direction, $L_p \sim 100$ km in the present setup, and tends to zero in the direction perpendicular to the background wind, where U_0 tends to zero. This explains why the new metrics is able to detect the PA-mediated response over short spatial scales. If the focus is on larger spatial scales, of the order of the PA adjustment scale $L_p \sim 100$ km, also smoothing the SST Laplacian and the wind divergence fields can recover the correlation. Notice also that this extends the findings of Lambaerts et al. (2013) to higher background wind conditions and confirms the results of Foussard et al. (2019).

An example of application of this new metrics to high-resolution satellite data in the Mediterranean Sea shows that by looking at the across-wind direction, we are able to detect a signal even with remote sensing observational products. It also shows that the PA mechanism is actually affecting the wind response over very short time scales, which, to the best of our knowledge, has never been found before. Future efforts will be devoted to characterize the spatio-temporal variability of the PA-mediated response using this kind of high-resolution satellite data.

Acknowledgments

The authors acknoweldge support from the project JPI Climate Oceans EUREC4A-OA, Progetto Dipartimenti di Eccellenza, funded by MIUR 2018-2022. A. N. M. is supported by the European Space Agency (ESA) as part of the Climate Change Initiative (CCI) fellowship (ESA ESRIN/Contract No. 4000133281/20/I/NB). F. D. is supported by ESA contract n. 4000127657/19/NL/FF/gp and by HPC-TRES grant number 2020-10. The WRF model outputs of interest can be downloaded from `https://10.5281/zenodo.5534306` The L4 ESA CCI SST analysis product v2.1 (Good et al., 2019) is available from the Centre for Environmental Data Analysis (CEDA) archive (accessible, for example, from `https://dap.ceda.ac.uk/neodc/esacci/sst/data/CDR_v2/`). The L2 coastal ASCAT METOP-A CDR wind field product (Verhoef et al., 2017) is available from the NASA JPL PO-DAAC platform (`https://podaac.jpl.nasa.gov/`).

References

Chelton, D. B., Esbensen, S. K., Schlax, M. G., Thum, N., Freilich, M. H., Wentz, F. J., ... Schopf, P. S. (2001). Observations of coupling between surface wind stress and sea surface temperature in the eastern tropical Pacific. *Journal of Climate*, *14*(7), 1479–1498.

Chelton, D. B., Schlax, M. G., Freilich, M. H., & Milliff, R. F. (2004). Satellite measurements reveal persistent small-scale features in ocean winds. *Science*, *303*(5660), 978–983.

Chelton, D. B., & Xie, S.-P. (2010). Coupled ocean-atmosphere interaction at oceanic mesoscale. *Oceanography*, *23*(4), 52-69. doi: 10.5670/oceanog.2010.05

Debreu, L., Marchesiello, P., Penven, P., & Cambon, G. (2012). Two-way nesting in split-explicit ocean models: Algorithms, implementation and validation. *Ocean Modelling*, *49*, 1-21. doi: 10.1016/j.ocemod.2012.03.003

Desbiolles, F., Alberti, M., Hamouda, M. E., Meroni, A. N., & Pasquero, C. (2021). Links between sea surface temperature structures, clouds and rainfall: Study case of the Mediterranean Sea. *Geophysical Research Letters*, *48*. doi: 10.1029/2020GL091839

Foussard, A., Lapeyre, G., & Plougonven, R. (2019). Response of surface wind diver-

gence to mesoscale SST anomalies under different wind conditions. *Journal of the Atmospheric Sciences*, *76*(7), 2065–2082.

Frenger, I., Gruber, N., Knutti, R., & Münnich, M. (2013). Imprint of southern ocean eddies on winds, clouds and rainfall. *Nature Geoscience*, *6*(8), 608–612.

Gaube, P., Chickadel, C. C., Branch, R., & Jessup, A. (2019). Satellite observations of SST-induced wind speed perturbation at the oceanic submesoscale. *Geophysical Research Letters*, *46*, 2690-2695. doi: 10.1029/2018GL080807

Good, S. A., Embury, O., Bulgin, C. E., & Mittaz, J. (2019). *ESA Sea Surface Temperature Climate Change Initiative (SST_cci): Level 4 Analysis Climate Data Record, version 2.1.* doi: 10.5285/62c0f97b1eac4e0197a674870afe1ee6. (Centre for Environmental Data Analysis)

Hayes, S., McPhaden, M., & Wallace, J. (1989). The influence of sea-surface temperature on surface wind in the eastern equatorial Pacific: Weekly to monthly variability. *Journal of Climate*, *2*(12), 1500–1506.

Kilpatrick, T., Schneider, N., & Qiu, B. (2014). Boundary layer convergence induced by strong winds across a midlatitude SST front. *Journal of Climate*, *27*, 1698-1718. doi: 10.1175/JCLI-D-13-00101.1

Lambaerts, J., Lapeyre, G., Plougonven, R., & Klein, P. (2013). Atmospheric response to sea surface temperature mesoscale structures. *Journal of Geophysical Research: Atmospheres*, *118*(17), 9611–9621.

Li, Y., & Carbone, R. (2012). Excitation of rainfall over the tropical western pacific. *Journal of the atmospheric sciences*, *69*(10), 2983–2994.

Lindzen, R. S., & Nigam, S. (1987). On the role of sea surface temperature gradients in forcing low-level winds and convergence in the tropics. *Journal of the Atmospheric Sciences*, *44*(17), 2418–2436.

Ma, Z., Fei, J., Lin, Y., & Huang, X. (2020). Modulation of clouds and rainfall by tropical cyclone's cold wakes. *Geophysical Research Letters*, *47*. doi: 10.1029/2020GL088873

Merchant, C. J., Embury, O., Bulgin, C. E., Block, T., Corlett, G. K., Fiedler, E., ... Donlon, C. (2019). Satellite-based time-series of sea-surface temperature since 1981 for climate applications. *Scientific Data*, *6*, 223. doi: 10.1038/s41597-019-0236-x

Meroni, A. N., Giurato, M., Ragone, F., & Pasquero, C. (2020). Observational evidence of the preferential occurrence of wind convergence over sea surface temperature fronts in the mediterranean. *Quarterly Journal of the Royal Meteorological Society*, *146*(728), 1443–1458.

Meroni, A. N., Parodi, A., & Pasquero, C. (2018). Role of sst patterns on surface wind modulation of a heavy midlatitude precipitation event. *Journal of Geophysical Research: Atmospheres*, *123*(17), 9081–9096.

Meroni, A. N., Renault, L., Parodi, A., & Pasquero, C. (2018). Role of the oceanic vertical thermal structure in the modulation of heavy precipitations over the ligurian sea. *Pure & Applied Geophysics*, *175*(11).

Minobe, S., Kuwano-Yoshida, A., Komori, N., Xie, S.-P., & Small, R. J. (2008). Influence of the gulf stream on the troposphere. *Nature*, *452*(7184), 206–209.

Penven, P., Debreu, L., Marchesiello, P., & McWilliams, J. C. (2006). Evaluation and application of the ROMS 1-way embedding procedure to the central California upwelling system. *Ocean Modelling*, *12*, 157-187. doi: 10.1016/j.ocemod.2005.05.002

Press, W. H., Teukolsky, S. A., Flannery, B. P., & Vetterling, W. T. (1992). *Numerical recipes in C* (2nd ed.). Cambridge University Press.

Redelsperger, J.-L., Bouin, M.-N., Pianezze, J., Garnier, V., & Marié, L. (2019). Impact of a sharp, small-scale SST front on the marine atmospheric boundary layer on the Iroise Sea: Analysis from a hectometric simulation. *Quarterly Journal of the Royal Meteorological Society*, *145*, 3692-3714. doi: 10.1002/qj.3650

Renault, L., Masson, S., Oerder, V., Jullien, S., & Colas, F. (2019). Disentangling the mesoscale ocean-atmosphere interactions. *Journal of Geophysical Research: Oceans*, *124*(3), 2164-2178. Retrieved from `https://agupubs.onlinelibrary.wiley.com/doi/abs/10.1029/2018JC014628` doi: 10.1029/2018JC014628

Skamarock, W. C., Klemp, J. B., Dudhia, J., Gill, D. O., Barker, D. M., Huang, X.-Y., ... Powers, J. G. (2008). A description of the Advanced Research WRF Version 3. *NCAR Technical Note NCAR/TN-475+STR*, 113. doi: 10.5065/D68S4MVH

Skyllingstad, E. D., de Szoeke, S. P., & O'Neill, L. W. (2019, 05). Modeling the transient response of tropical convection to mesoscale SST variations. *Journal of the Atmospheric Sciences*, *76*(5), 1227-1244. doi: 10.1175/JAS-D-18-0079.1

Skyllingstad, E. D., Vickers, D., & Mahrt, L. (2007). Effects of mesoscale sea-surface temperature fronts on the marine atmospheric boundary layer. *Boundary Layer Meteorology*, *123*, 219-237. doi: 10.1007/s10546-006-9127-8

Small, R., DeSzoeke, S., Xie, S., O'Neill, L., Seo, H., Song, Q., ... Minobe, S. (2008). Air-sea interaction over ocean fronts and eddies. *Dynamics of Atmospheres and Oceans*, *45*(3), 274–319.

Spall, M. A. (2007). Midlatitude wind stress–sea surface temperature coupling in the vicinity of oceanic fronts. *Journal of Climate*, *20*(15), 3785–3801.

Takatama, K., Minobe, S., Inatsu, M., & Small, R. J. (2015). Diagnostics for near-surface wind response to the Gulf Stream in a regional atmospheric model. *Journal of Climate*, *28*, 238-255. doi: 10.1175/JCLI-D-13-00668.1

Verhoef, A., Vogelzang, J., Verspeek, J., & Stoffelen, A. (2017). Long-term scatterometer wind climate data records. *IEEE Journal of Selected Topics in Applied Earth Observations and Remote Sensing*, *10*(5), 2186-2194. doi: 10.1109/JSTARS.2016.2615873

Wallace, J. M., Mitchell, T., & Deser, C. (1989). The influence of sea-surface temperature on surface wind in the eastern equatorial Pacific: Seasonal and interannual variability. *Journal of Climate*, *2*(12), 1492–1499.

Wenegrat, J. O., & Arthur, R. S. (2018). Response of the atmospheric boundary layer to submesoscale sea surface temperature fronts. *Geophysical Research Letters*, *45*, 13505-13512. doi: 10.1029/2018GL081034